ADVANCED OPTICAL MATERIALS
www.advopticalmat.de

High-Efficiency Multi-Level Beam Switching with Single-Gate Tunable Metasurfaces Based on Graphene

*Juho Park, Ju Young Kim, Sunghyun Nam, and Min Seok Jang**

The growing demand for ultra-fast telecommunications, autonomous driving, and futuristic technologies highlights the crucial role of active beam steering at the nanoscale. This is essential for applications like LiDAR, beam-forming, and holographic displays, especially as devices reduce in form factor. Although a device with active beam-switching capability is a potential candidate for realizing those applications, there are only a few works to realize beam switching in reconfigurable metasurfaces with active tuning materials. In this paper, a multi-level beam-switching dielectric metasurface is theoretically presented with a graphene layer for active tuning, addressing challenges associated with achieving high directivity and diffraction efficiency, and doing so while using a single-gate setup. For two-level switching, the directivities reached above 95%, and the diffraction efficiencies are ≈50% at the operation wavelength $\lambda_0 = 8$ µm. Through quasi-normal mode expansion, the physics of the beam-switching metasurface inverse-designed by the adjoint method is illustrated, highlighting the role of resonant modes and their response to charge carrier tuning. Under the same design scheme, characteristics of a three-level and four-level beam-switching device is designed and reported, suggesting a possibility of generalizing to multi-level beam switching.

1. Introduction

As the demand for ultra-fast telecommunications, autonomous driving, and other futuristic technologies continues to grow, the need for wavefront shaping capability at the micro-scale has become more evident.[1–4] Metasurfaces, consisting of subwavelength dielectric or plasmonic components, are suitable candidates for realizing complex light manipulations. To date, many metasurface designs have been static, i.e. the geometric and optical parameters of the underlying components are fixed after fabrication. However, advanced optical applications, such as LiDAR,[5] tunable metalenses,[6] wavefront shapers,[7] and holographic displays for virtual/augmented reality,[8] need active/reconfigurable metasurfaces that can be tuned dynamically. Active beam-switching is one such application.

To enable such active beam-switching, various forms of reconfigurable metasurfaces have been suggested,[9] with the tuning mechanisms spanning electro-optic, thermo-optic, and mechanical modulations. Solid state methods, such as charge carrier tuning, is optimal for the reasons of local controllability and robustness, while on the other hand using a dielectric meta-atom platform is preferred over the usage of metallic components, which has significant ohmic dissipations. These conditions naturally pinpoint to the usage of a dielectric platform with a charge carrier-tunable 2D material, which has a minimal volume that is lossy, yet is required for the active tuning. Among these, graphene charge carrier tuning is a favorable candidate for active tuning in reconfigurable metasurfaces, owing to graphene's atomic layer thickness and high electrostatic tunability.[10–13] There have been various demonstrations of active metasurfaces highlighting graphene's promising tuning capability, such as active thermal emission control[14,15] and high-efficiency independent modulation of phase and amplitude.[16,17] The tuning speed, or the switching rate, of the GHz range in graphene[18] is also superior to that of the other methods such as the usage of liquid crystals, which only has a switching rate in the KHz range.[19]

Given the active tuning method, there are various ways of designing the metasurface for manipulating the wavefront into desired diffraction orders. Generally speaking, these can be categorized into bottom-up methods and top-down methods. Bottom-up methods include the unit-cell method, which spatially arranges designated meta-atoms according to the required phase profile.[20] For the designing of active metasurfaces, a unit-cell method often requires a multi-gated setup for dynamically tuning each meta-atom separately according to the desired beam deflecting angle, leading to a complex experimental arrangement.[17,21] Also, it is widely known that metasurfaces designed by the unit-cell method likely yield limited efficiencies due to the anticipated mode profiles of the unit cells overlapping with the neighboring ones, leading to a significant deviation from the locally periodic approximation and resulting in undesired wavefronts.[22,23] This

J. Park, J. Y. Kim, S. Nam, M. S. Jang
School of Electrical Engineering
Korea Advanced Institute of Science and Technology
Daejeon 34141, Republic of Korea
E-mail: jang.minseok@kaist.ac.kr

The ORCID identification number(s) for the author(s) of this article can be found under https://doi.org/10.1002/adom.202500236

DOI: 10.1002/adom.202500236

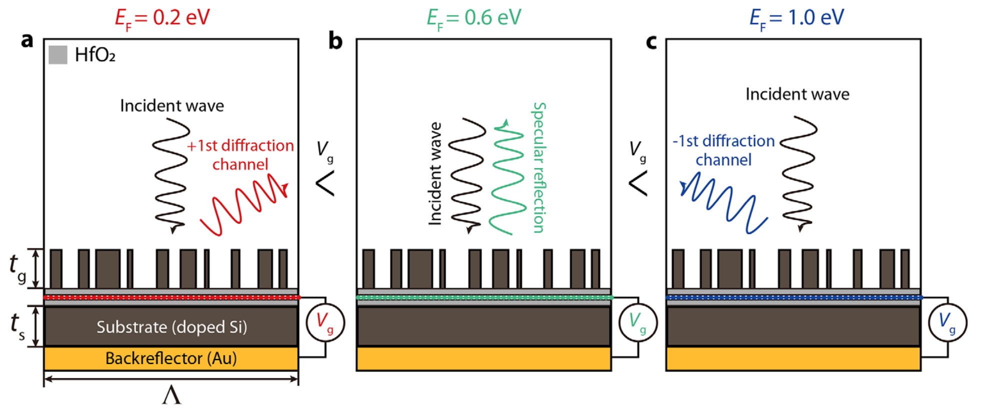

Figure 1. Schematic of the three-level beam switching metasurface and the switching mechanism. The free-form metal grating is located above the unpatterned graphene layer, serving as a resonant coupler, guiding normal incident waves into different diffraction channels. The gate voltage is applied between the Au back reflector and the unpatterned graphene. As the gate voltage increases, the metasurface switches the reflection of the normally incident plane wave into a) +1st diffraction order, b) 0th diffraction order, and c) −1st diffraction order. There is a thin HfO_2 etch-stop layer between the metal grating and graphene layer. A thin HfO_2 spacer is embedded between the doped Si substrate and the graphene layer, as a gate dielectric.

phenomenon is aggravated in cases requiring abrupt metasurface fields manipulations, such as implementing high numerical aperture in metalenses or large beam diffraction angles in metal gratings.[24] Nevertheless, due to its simple design procedure and modeling capabilities, it is prominently used in many metasurface design works.[25–28] On the opposing end, the top-down, holistic design methods use nonlocalized modes to enable high-efficiency beam diffraction under abrupt field manipulation,[29] incorporating the overlapping field effects between neighboring meta-atom components. The top-down methods include adjoint-based topology optimization[30] or deep-learning-based methods.[31] There are numerous publications regarding high-performance beam-deflecting metasurfaces designed by these methods.[32–36]

Among the numerous qualities of beam-switching metasurfaces, we focus on satisfying the key performance metrics simultaneously, namely the high beam diffraction angle, high directivity, and diffraction efficiency for multi-level switching. Designing a dynamic high-angle beam-switching metasurface compounds the complexities, and we overcome the associated difficulties by using holistic methods. We observed that the current state-of-the-art active beam-switching metasurfaces require a multi-gated setup or have low beam diffraction angles. In this paper, we aim to design a metasurface that improves those aspects, so that the needs of achieving high directivities/efficiencies for high beam switching angles, using a single-gated setup, and implementing multi-level beam switching are all met. Our metal grating setup is a dielectric one, with a graphene layer for active tuning purposes, which minimizes energy loss while keeping the freedom to significantly tune charge carriers. Utilizing the adjoint-based holistic optimization method, we first demonstrate a two-level beam-switching metasurface, for the sake of simply illustrating the physics of our metal grating, which involves the utilization of different quasinormal modes (QNMs) and how they respond to the charge carrier tuning. The pole-zero analysis and QNM expansion method are used to trace the trajectories of these resonances through the corresponding poles and elucidate their roles in beam switching.[37] Finally, as a trial toward generalized multi-level beam switching, we move on to the design of a 3- and 4-level beam switching device, where the principles behind how the different QNMs enable the beam switching are similar but involve more QNMs.

2. Results and Discussion

2.1. Metasurface Configuration

In this section, we propose a reflective active beam-switching metasurface utilizing unpatterned graphene as a tuning material. **Figure 1** illustrates the unit-cell structure of the three-level switching metasurface and beam switching operation. The structure consists of a Si metal grating with thickness t_g, an unpatterned graphene layer, a hafnia (HfO_2) spacer and an etch-stop layer with thicknesses t_{spacer} and $t_{etch\text{-}stop\text{-}layer}$ respectively, a lightly doped Si substrate with thickness t_s, and an Au back reflector. The period is set to $\Lambda = \lambda_0/\sin(\theta)$ in order to eliminate higher diffraction orders and force the +1st and -1st diffraction orders to have diffraction angles of $\pm\theta$, where $\theta = 80°$ throughout this paper. The incident plane wave is transverse-electric (TE) polarized to minimize the ohmic losses in the back reflector. The operating wavelength is set to $\lambda_0 = 8$ µm, which causes both carrier intraband and interband transition in graphene within our Fermi energy range of interest.[38]

Each constitutive layer has its own purpose in enabling the active beam-switching functionality of the metasurface. The Si metal grating, the principal region to be optimized, acts as a coupling interface that connects the normally incident plane waves into desired diffraction orders. To prevent damage to the unpatterned graphene when etching the Si metal grating patterns, the thin HfO_2 etch-stop layer was embedded above the graphene. As a gate dielectric for preventing electrical shorts, the thin HfO_2 spacer is inserted between the graphene layer and Si substrate. The Au back reflector enhances the light-matter interaction by doubling the light path. The graphene and the Au back reflector are connected to apply gate biases (V_g). Upon different applied gate voltages, the three-level beam switching metasurface reflects the incident plane wave into either +1st (**Figure 1a**), 0th (Figure 1b), or -1st (Figure 1c) diffraction channels.

Here, we explain the selection of the materials and the thicknesses of each layer considering experimentally realizable conditions. We expect the proposed metasurface can be fabricated through the current nanofabrication process, especially utilizing the deep reactive ion etching (DRIE) technique[39] to pattern the Si metal grating layer. In this work, we conservatively set the highest aspect ratio of the Si pillars (trenches) to 10, which is far below the aspect ratios that DRIE can achieve, which, reportedly are above 100.[40] For the etch-stop layer, a 50 nm-thick HfO_2 was employed owing to its high etch resistance and selective etching properties.[41,42] In order to realize feasible gate voltages, we use lightly doped Si as a substrate, and HfO_2 as a gate dielectric. For the substrate, the lightly doped Si has doping concentrations lower than 10^{15} cm^{-3}, which are low enough to maintain transparency in the mid-infrared regime due to negligible free-carrier absorption but high enough to enable electrical gating.[43] For the gate dielectric, HfO_2 is a good candidate as it has a high dielectric constant.[44] We set the thickness of the HfO_2 spacer as $t_{spacer} = 30$ nm. As a result, one can obtain Fermi levels of 0.2, 0.6, and 1.0 eV with the gate voltages of 0.9, 8, and 22 V relative to the Dirac voltage $|V_g - V_{Dirac}|$, respectively, which are well under the breakdown voltage of HfO_2.[45] (see Section S1, Supporting Information).

2.2. Inverse Design of Two-Level Beam Switching Metasurface

To gain an insight into how active beam switching works, we first demonstrate a two-level beam-switching metasurface. For the two-level beam-switching metasurface, the unit-cell period is set to Λ, and the Fermi energy switching levels are 0.2 and 0.6 eV, respectively. To achieve a clear plane wavefront with high deflection, we utilize the adjoint method as a design strategy.

Along with classical optimization methods[46,47] and deep-learning-based design methods,[48,49] the adjoint method is prevalently used for many photonic inverse design problems,[34,50,51] owing to its efficient evaluation of the FoM (figure of merit) gradient upon design parameters. Specifically, it enables the calculation of the FoM gradient using only two simulations, forward and adjoint simulations, regardless of the number of design parameters.[52,53] A more detailed explanation of the adjoint gradient formulation is given in Section S2 (Supporting Information). There are two types of adjoint gradients. One is the grayscale gradient which is the gradient when the permittivity value changes while the shape is fixed. The other is the shape-derivative which is the gradient when the shape changes while the permittivity is fixed. Deploying the shape-derivative instead of the grayscale adjoint gradient[50] enables one to naturally control the highest aspect ratio, by integrating it as a constraint to the optimization problem. As mentioned in Section 2.1, in this work, we set the highest aspect ratio of Si pillars to be 10, which is realizable under the use of contemporary etching techniques used in mass production, including deep reactive ion etching.[39]

For beam switching/steering applications, diffraction efficiency is an important characteristic as it is directly related to the energy efficiency of the device. Also, beam directivity is a crucial factor as it is directly related to beam divergence and spatial resolution.[21,54] Therefore, it is important for a beam-switching metasurface to maximize both performance metrics simultaneously. Throughout this paper, we denote the diffraction efficiency into ith diffraction channel as R_i, as there is no transmission through the metasurface. Directivity is defined as the ratio of the diffraction efficiency into the target diffraction channel (R_{target}) divided by sum of diffraction efficiencies: $D_{target} = R_{target}/\sum_i R_i$.To satisfy high directivities and high diffraction efficiencies for all switching states, we define the total FoM to be maximized as follows:

$$\mathrm{FoM} = \sum_{\mathrm{states}} \left(bR_{\mathrm{target}} - \sum_{i=\mathrm{off-target}} R_i \right) \tag{1}$$

where b is a trade-off coefficient, having a positive value. Setting the trade-off coefficient b to be small relatively puts less weight on the target diffraction efficiency and more weight on the off-target efficiencies. In this case, the optimizer emphasizes minimizing the off-target diffraction efficiencies (due to the minus sign in the FoM) at the expense of maximizing the target diffraction efficiency, leading to a high directivity as the off-target diffraction efficiencies are greatly minimized but with the cost of a slightly lower target diffraction efficiency for each switching state. On the other hand, a higher b value relatively puts a heavier weight on the target diffraction efficiency and less on the off-target efficiencies. This results in a high target diffraction efficiency but low directivity. The effect of varying the trade-off coefficient b is visualized in Section S11 (Supporting Information). Balancing this trade-off, we subtly tune b to 0.3 in order to achieve both high directivity and diffraction efficiencies.

Using the aforementioned optimization procedures, we sweep the thicknesses of the metal grating layer t_g and substrate layer t_s from $k_{Si}t_g = \pi/8$ to 2π and $k_{Si}t_s = \pi/8$ to 2π with steps of $\pi/8$, where $k_{Si} = n_{Si}k_0$ and k_0 is the free-space wavevector at $\lambda_0 = 8$ µm. For each pair of (t_g, t_s), five optimizations were conducted with different initial points, leading to a total of 1280(= 256 × 5) optimizations. By examining the sweep results, we found that there exist "forbidden zones" that prevent achieving both high diffraction efficiencies and directivities, comprehensively analyzed in Section S3 (Supporting Information). Interestingly, for two, three, and four-level beam switching device optimizations, the designs with both high directivities and high diffraction efficiencies were often located near the point of $(k_{Si}t_g, k_{Si}t_s) = (3\pi/2, 3\pi/2)$. Therefore, throughout this paper, we report the case of $t_g = t_s = 3\pi/(2k_{Si}) = 1.75$ µm.

It is worthwhile to note that since our optimization algorithm is based on a gradient-descent algorithm, each optimization result (solution) depends on its initial point. However, for the two- and three-level metasurfaces, with many different initial points, the optimal solution converged to comparable performances to the metasurface designs we report here. For the four-level switching metasurface, the FoM landscape became noisier, which made the optimization problem harder, often leading to designs much inferior to the performance we report here. We did not use any pre-optimization steps to improve the quality of our initial points.

Figure 2 depicts the geometrical structure of the optimized metasurface and the optical responses. The unit cell structure of the optimized two-level beam-switching metasurface is shown in Figure 2a. The exact geometric parameters of optimized

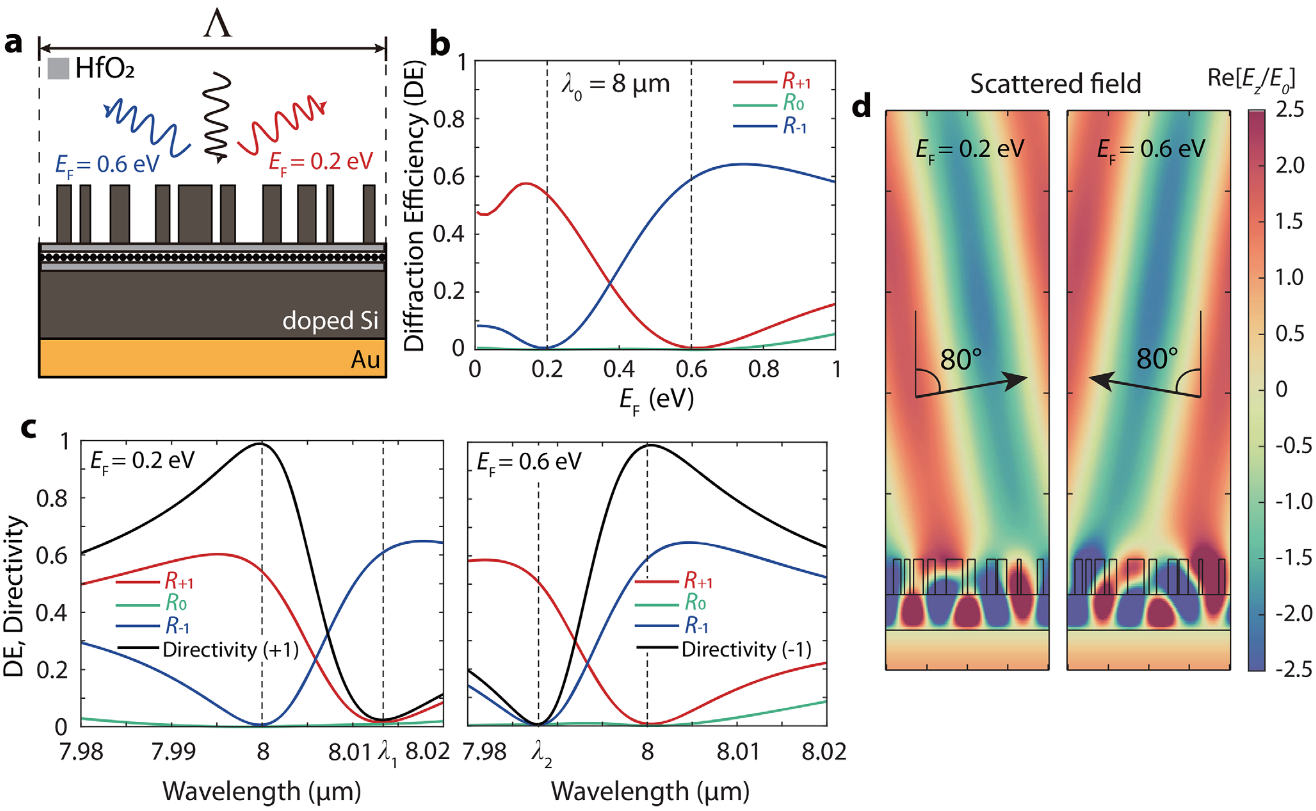

Figure 2. Optimization result of two-level beam switching device. a) Unit-cell structure of the optimized two-level beam switching metasurface. Sizes are not to scale. b) DEs of +1st (red solid line), 0th (green solid line), and −1st (blue solid line) diffraction orders at $\lambda_0 = 8$ µm, along graphene Fermi levels. The vertical dotted lines indicate the two switching Fermi levels, $E_F = 0.2$ eV, and 0.6 eV. c) DEs of +1st (red solid line), 0th (green solid line), and −1st (blue solid line) diffraction orders, and directivity (black solid line) for Fermi levels $E_F = 0.2$ eV (left) and 0.6 eV (right), along wavelengths. The vertical dotted lines indicate the zeros of DEs for +1st and −1st diffraction orders, $\lambda_1 = 8.0132$ µm and $\lambda_2 = 7.9876$ µm, respectively. d) Real part of scattered electric field for $E_F = 0.2$ eV (left) and 0.6 eV (right), normalized by the electric field amplitude of the incident plane wave. The angles of wavefronts coincide with the diffraction angles of 80° (+1st) and −80° (−1st). The outlines of the structure are shown in black lines.

metal grating patterns for two-, three-, and four-level switching metasurfaces are shown in Section S4 (Supporting Information). At $E_F = 0.2$ eV the optimized metasurface shows directivity and diffraction efficiency (DE) being 98.8% and 54.1%, respectively, and at $E_F = 0.6$ eV, 98.9% and 58.9%, respectively. The diffraction efficiencies along different graphene Fermi levels at the operating wavelength $\lambda_0 = 8$ µm are shown in Figure 2b, whereas Figure 2c shows the DEs for different wavelengths at two switching states. The scattered electric field simulated by the FEM solver reveals clear wavefronts toward the target directions (Figure 2d). The angles of the formed wavefronts manifest in ±80° which correspond to desired diffraction angles.

Here, we focus on the observation that the diffraction efficiency spectrum (comparing the left and right figure of Figure 2c) for $E_F = 0.6$ eV is similar to the one for $E_F = 0.2$ eV, with the zeros of diffraction efficiencies for the +1st and −1st diffraction channels having been moved from 8 µm and $\lambda_1 = 8.0132$ µm ($E_F = 0.2$ eV) to $\lambda_2 = 7.9876$ µm and 8 µm ($E_F = 0.6$ eV), respectively. Also, the dependence of reflectance on the Fermi levels is like the dependence on the wavelengths (comparing Figure 2b and Figure 2c). The similarity can be explained by investigating the resonance frequency tuning mechanism. From perturbation theory,[55] the resonance frequency shift $\Delta\omega$ can be approximated to the first-order, leading to:

$$\Delta\omega = -\frac{\omega_0}{2}\frac{\int dv\,\Delta\varepsilon\,(r)\,|E\,(r)|^2}{dv\,\varepsilon\,(r)\,|E\,(r)|^2} \tag{2}$$

where ω_0 and $E(\mathrm{r})$ are the mode resonance frequency and its electric field, respectively, and $\epsilon(\mathrm{r})$ and $\Delta\epsilon(\mathrm{r})$ are the permittivity distribution and its change due to active control, respectively. The integral operator is applied to the whole region of the unit cell. In our case, the active control parameter corresponds to the Fermi level of graphene. As the Fermi level changes, changes in permittivity occur only in the active material region, i.e. unpatterned graphene layer. Also, the electric fields are dispersed over a larger area of the whole metasurface, unlike the case of graphene plasmons, which involve extremely highly concentrated electric fields around the graphene regions.[16] Therefore, the field intensities are "weak" enough for the first-order perturbation approximation Equation (1) to uphold, which results in the resonance frequency shift $\Delta\omega$ being roughly proportional to the changes in permittivity $\Delta\epsilon$. Despite the nonlinearity in the dependence of graphene $\Delta\epsilon$ on the Fermi level change ΔE_F,[12] the actual plot of the complex $\Delta\epsilon$ on ΔE_F yields a linear-looking curve at $\lambda_0 = 8$ µm, room temperature, and mobility values of 500–2000 cm^2 $V\cdot^{-1}s$ (see Section S5, Supporting Information). As a result, the resonance frequency shift $\Delta\omega$ shows almost linearly proportional behavior to the Fermi level change ΔE_F, i.e. $\Delta\omega \propto \Delta\epsilon \propto \Delta E_F$. This linear resonance frequency shift with respect to the graphene Fermi level has also been observed in quasi-bound states in the continuum (qBIC) tuning in unpatterned graphene-based metasurfaces.[16] Since this linear resonance frequency shift occurs continuously while preserving the resonance lineshapes, the diffraction efficiency spectrum drawn as a function of λ (Figure 2c) consequently resembles the one drawn as a function of E_F (Figure 2b).

In Section S10 (Supporting Information), we further report the optimization results of two- and three-level beam-switching metasurfaces for λ_0 = 7, 7.5, 8.5, and 9 µm. For those wavelengths, the directivities and diffraction efficiencies were comparable to λ_0 = 8 µm, indicating our approach can be extended to a broader frequency range.

2.3. Quasinormal Mode Expansion of Reflection Coefficients

In this section, we analyze the reflection coefficients of each diffraction order in the two-level beam-switching metasurface, by expanding them as a sum of the contributions of intrinsic QNMs. A QNM refers to an eigenmode when the system is open and non-Hermitian, in the presence of incoming and outgoing radiation channels and lossy materials in the system.[56] QNM mode expansion technique is a popular tool for investigating nanophotonic devices,[57–60] owing to its capability of clearly identifying each QNM's contribution to certain optical responses. To illuminate how each of the QNMs, alongside the continuous radiation spectrum that they are coupled to, contributes to the spectrum of interest, we utilize the Riesz Projection (RP) method. The RP method is a type of QNM expansion. The RP method is able to identify the contributions of each resonant QNM to a given spectrum, while also being able to identify the contribution from the non-resonant background mode.[61] Additionally, the RP method has several advantages compared to other QNM expansion methods. First, the RP method does not require prior knowledge of the exact shape of eigenmodes, only the knowledge of eigenfrequencies. Second, it does not depend on orthogonality relations and is free from normalization issues. Third, it is based on contour integration, so the contributions of each mode can be related by a simple summation.[59,62] A brief formulation of the RP method is addressed in Section S6 (Supporting Information).

As the RP method needs evaluations of optical responses in the complex frequency plane, we used an open-source rigorous coupled-wave analysis (RCWA) solver Section S4 (Supporting Information).[63] The material properties used for Si (substrate), HfO_2 (spacer and etch-stop layer), and Au (back reflector) have been analytically extended to the complex plane by inserting complex frequency into their Drude-Lorentz model permittivity formula.[64] The conductivity of graphene has been analytically extended by using the conductivity model,[65] which represents the conductivity as a function of frequency, temperature, and carrier density.

Before applying the QNM expansion, we first analyze the locations of the poles and zeros of +1st, 0th, and −1st diffraction coefficients, denoted as r_{+1}, r_0, and r_{-1}, respectively, in the complex frequency plane as a function of Fermi levels. **Figure 3a** illustrates the trajectories of the poles and zeros in the two-level beam-switching metasurface. These poles and zeros locations are first estimated by a brute-force sweep in the complex frequency plane, and fine-tuned by local root-finding algorithms.[66,67] The pole locations are denoted by ω_{pn}, where n is the index of the poles numbered from low Re{ω}. The zero locations are denoted by $\omega_{zn,m}$, where n is the index of the zeros numbered from low Re{ω}, and m represents the corresponding diffraction order. We note that the trajectories of zeros whose locations are far from the real frequency axis have been omitted in Figure 3a and Figure 4b,d, as they are less relevant to the switching mechanism. For the full locations of the trajectories, see Section S7 (Supporting Information).

As the graphene Fermi level increases, all the poles and zeros tend to blueshift. The linear shift of poles (resonances) along increasing Fermi levels is an expected behavior that is predicted by Equation (1), due to the changes in the relatively small volume of graphene (2D layer) acting as a perturbation. The linear shift of zeros is intricately linked to the linear shift of poles, as the positions of both zeros and poles are constrained by causality and energy conservation. Because the poles move linearly according to Equation (1), it is natural for the zeros to shift linearly as well, as the Kramers-Kronig relations relate the two locations.

To achieve high directivities, all unwanted diffraction channels must be suppressed simultaneously by having zeros near the real target frequency $\omega_0 = 2\pi c/\lambda_0$, whereas all zeros of the target diffraction coefficient should be located far away from ω_0. For our optimized device, as shown in Figure 3a, $\omega_{z2,0}$ and $\omega_{z1,-1}$ are the two zeros located near ω_0 and very close to the real frequency axis at E_F = 0.2 eV, making the majority of the beam diffracted into the +1st order. Similarly, at E_F = 0.6 eV, $\omega_{z1,0}$ and $\omega_{z1,+1}$ are near ω_0, funneling incident light into the −1st order diffraction channel.

The complex pole-zero analysis also reveals that there exist two poles mainly involved in our frequency range of interest. The electric field profiles of the two QNMs corresponding to the two poles can be found in Section S8 (Supporting Information).

The QNM expansion illustrates how the two-level beam switching is achieved with the dynamics between these two QNMs and the background mode as displayed in Figure 3b. The physical observables that are decomposed into the algebraic sum of the modal contributions are the diffraction coefficients, which are complex values, so we show both their amplitude and the phase.

As discussed above, to achieve high directivity beam switching, the +1st and −1st order diffraction channels must be alternatively switched on and off depending on E_F, whereas the 0th order channel must be nulled for both E_F = 0.2 and 0.6 eV. For the +1st order diffraction channel, the combined response of mode 1 and mode 2 shows similar amplitude to the background diffraction amplitude and has exactly π phase difference to the background response, shown in Figure 3b, and therefore the destructive interference between the background and the combined mode response is nearly complete, nullifying the $+1^{st}$ diffraction channel at E_F = 0.6 eV. Through a similar destructive interference mechanism, the −1st diffraction channel is suppressed at E_F = 0.2 eV,

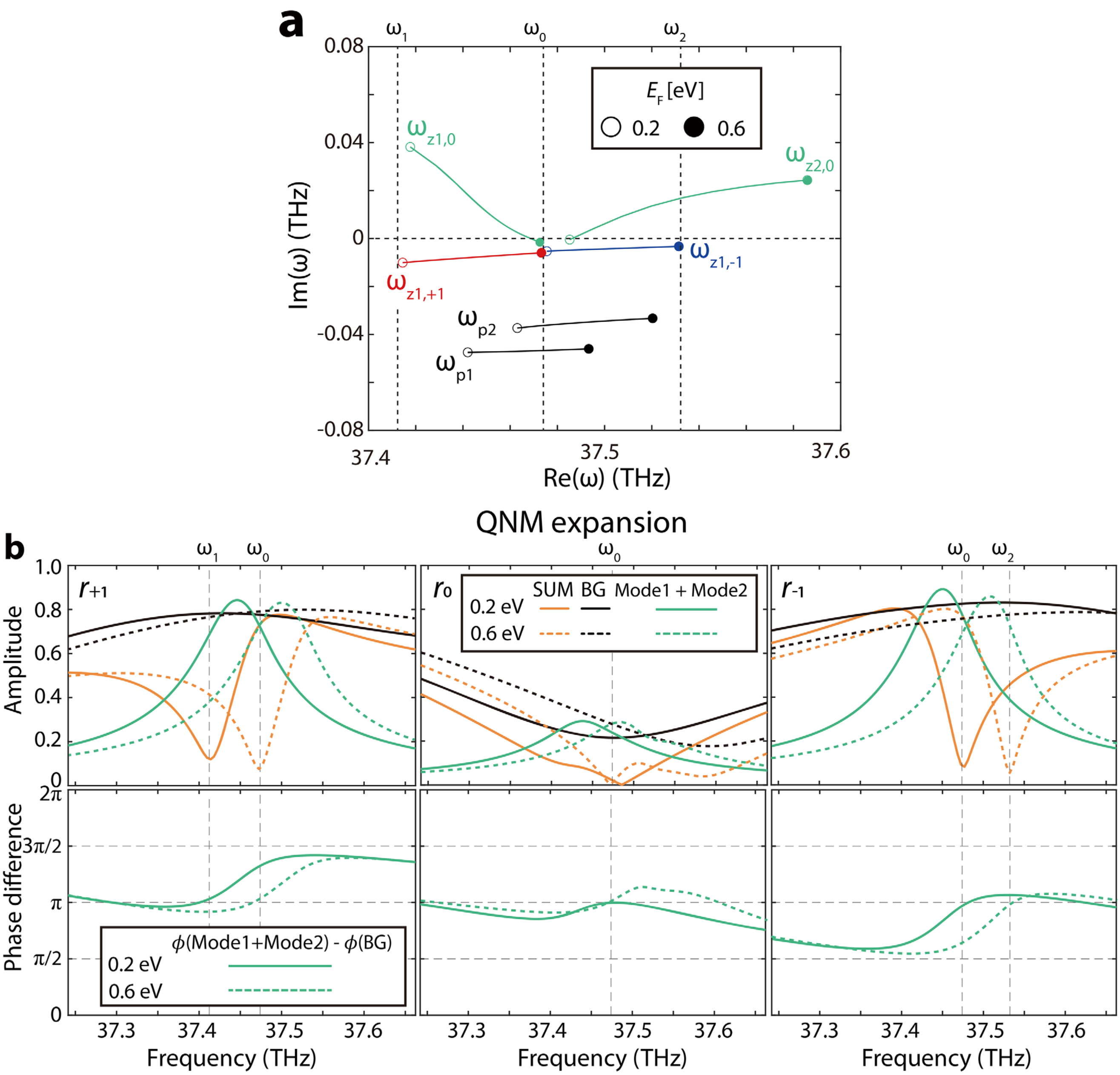

Figure 3. Complex frequency analysis and QNM decomposition of the two-level beam switching metasurface. a) The locations of poles and zeros, depending on continuous graphene Fermi level range of $E_F = 0.2$–0.6 eV. The poles are indicated by black lines. The zeros of +1st, 0th, −1st diffraction orders are indicated by red, green, and blue lines, respectively. The poles and zeros at $E_F = 0.2$ eV are indicated as empty circles, while at $E_F = 0.6$ eV are indicated as filled circles. The locations of frequencies ω_0, ω_1, and ω_2 which correspond to wavelength λ_0, λ_1, and λ_2 are indicated as vertical dotted lines. b) QNM expansions of reflection (diffraction) coefficients for $E_F = 0.2$ eV and $E_F = 0.6$ eV. For all subplots, solid and dotted lines are for $E_F = 0.2$ eV and $E_F = 0.6$ eV, respectively. The amplitude of the combined mode and its phase difference with respect to the background mode are drawn in the upper row and lower row, respectively. (Upper row) For each diffraction order, the combined mode of modes 1 and 2, and the background mode are drawn in green, and black curves, respectively. Summed quantities are drawn in yellow curves. (Lower row) Phase differences of the combined mode of modes 1 and 2, with respect to background mode, are drawn in green curves.

and the 0th diffraction channel is suppressed at both $E_F = 0.2$ eV and $E_F = 0.6$ eV. Here, we present the amplitude and phase of the combined mode only, to facilitate explaining the complex switching mechanism using QNM expansion. For the amplitude and phase information of individual modes 1 and 2, see Section S9 (Supporting Information).

2.4. Inverse Design of Three- and Four-Level Beam Switching Metasurfaces

As an extension to the two-level beam-switching metasurface, we design metal grating patterns to achieve three-level and four-level beam-switching capabilities. For the three-level switching, the

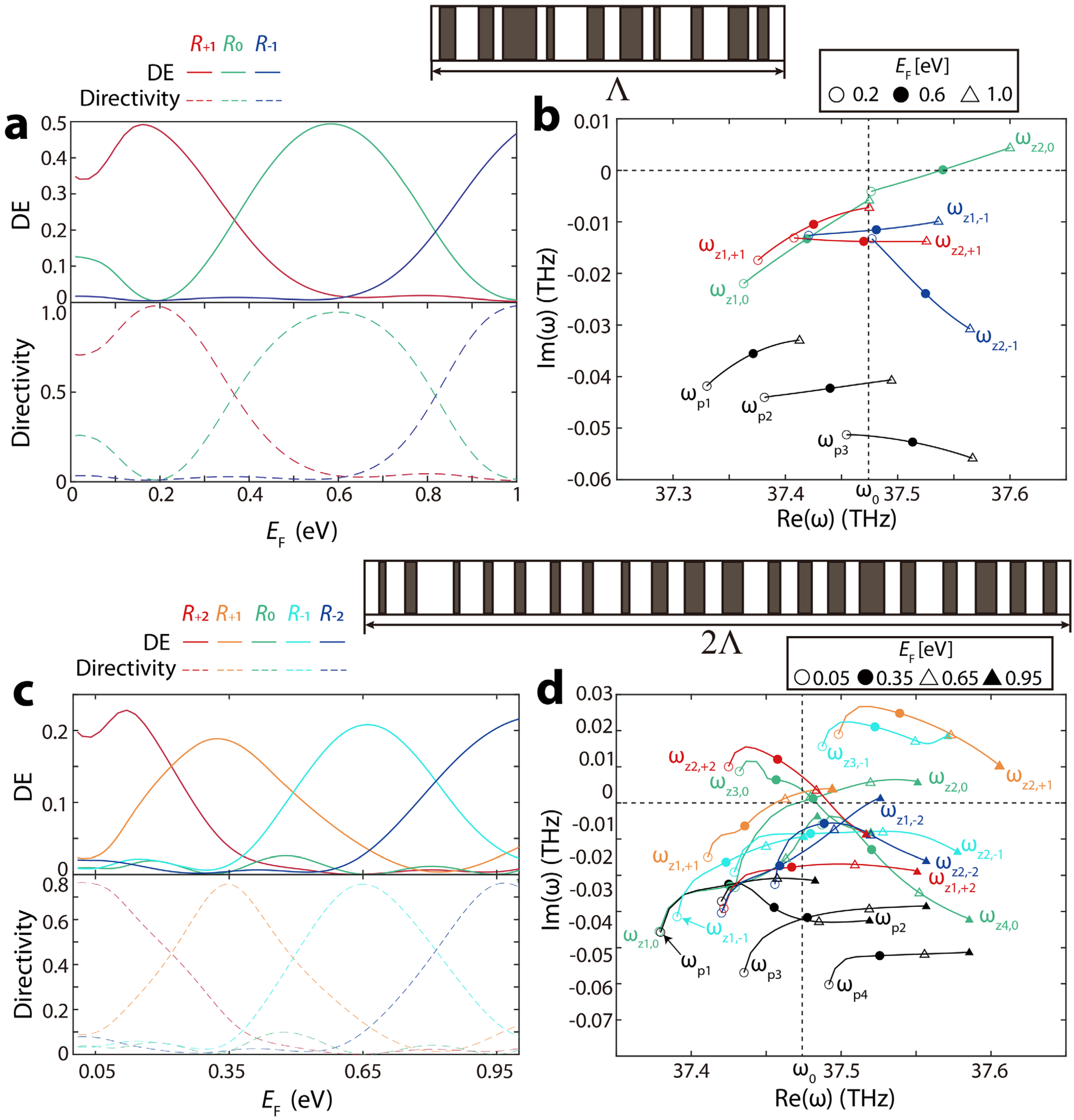

Figure 4. Multi-level beam switching metasurfaces. a) Diffraction efficiencies (upper row) and directivities (lower row) of the three-level beam switching metasurface, indicated by solid lines and dashed lines, respectively. Red, green, and blue lines correspond to the +1st, 0th, and −1st diffraction orders, respectively. b) The locations of poles and zeros, dependent on the graphene Fermi levels of E_F = 0.2–1.0 eV. The poles are indicated by black lines. The zeros of +1st, 0th, and −1st diffraction orders are indicated by red, green, and blue lines, respectively. The poles and zeros at E_F = 0.2, 0.6, and 1.0 eV are indicated as empty circles, filled circles, and empty triangles, respectively. c) Diffraction efficiencies (upper row) and directivities (lower row) of four-level beam switching metasurface, indicated by solid lines and dashed lines, respectively. Red, yellow, green, cyan, and blue lines correspond to the +2nd, +1st, 0th, −1st, and −2nd diffraction orders, respectively. d) The locations of poles and zeros, dependent on the graphene Fermi level range of E_F = 0.05–0.95 eV. The poles are indicated by black lines. The zeros of the +2nd, +1st, 0th, −1st, and −2nd diffraction orders are indicated by red, yellow, green, cyan, and blue lines, respectively. The poles and zeros at E_F = 0.05, 0.35, 0.65, and 0.95 eV are indicated as empty circles, filled circles, empty triangles, and filled triangles, respectively. The optimized metal grating patterns for the three-level and the four-level switching metasurfaces are shown above (a,b) and (c,d), respectively.

period is Λ, the same as in the two-level case. The Fermi levels of the switching states are set to E_F = 0.2, 0.6, and 1.0 eV for the +1st, 0th, and −1st diffraction orders, respectively. The optimized metal grating pattern is shown above in Figure 4a,b, exhibiting 97.8%, 94.6%, and 98.1% directivities and 47.5%, 49.2%, and 46.8% diffraction efficiencies for E_F = 0.2, 0.6, and 1.0 eV respectively, as shown in Figure 4a. The main difference between the two-level and the three-level beam-switching metasurface is that the three-level beam-switching one has three poles (QNMs). Also, the trajectories of the poles and zeros are more complicated than those of the two-level design, shown in Figure 4b. Here, the mechanism of alternating zeros and nonzeros along the switching levels is similar to the two-level switching metasurface. At E_F = 0.2 eV, $\omega_{z2,0}$ and $\omega_{z2,-1}$ crosses $\omega = \omega_0$, making R_0 and R_{-1} zero. At E_F = 0.6 eV, $\omega_{z2,+1}$ and $\omega_{z1,-1}$ crosses $\omega = \omega_0$, making R_{+1} and R_{-1} zero. At E_F = 1.0 eV, $\omega_{z1,+1}$ and $\omega_{z1,0}$ crosses $\omega = \omega_0$, making R_{+1} and R_0 zero.

For the four-level switching, the period is set to 2Λ, to have the extra −2nd and 2nd order diffraction channels. The Fermi levels for switching states are set to E_F = 0.05, 0.35, 0.65, and 0.95 eV for +2nd, +1st, −1st, and −2nd diffraction orders, respectively. The optimized metal grating pattern is displayed above Figure 4c,d and it shows ≈76% directivities for all four states and 19.4%, 18.6%, 20.8%, and 20.3% diffraction efficiencies for E_F = 0.05, 0.35, 0.65 and 0.95 eV, respectively, as shown in Figure 4c. In this case, as a large number of zeros and poles are involved, as shown in Figure 4d, it is difficult to clearly state the dynamics of the QNMs as in two- and three-level switching metasurfaces. Nevertheless, the general characteristics of poles and zeros remain similar for the four-level switching metasurface. For example, $\omega_{z2,+1}$, $\omega_{z4,0}$, $\omega_{z3,-1}$, and $\omega_{z2,-2}$ are the zeros located near $\omega = \omega_0$ to suppress R_{+1}, R_0, R_{-1}, and R_{-2} at E_F = 0.05 eV. We would like to point out that, unlike the application of phase-modulating metasurfaces, which require zeros *above* the real frequency line,[68,69] our application of beam steering requires zeros *on* the real frequency line. Also, similar to the cases of two- and three-level switching metasurfaces, the blueshift of zeros and poles remains the same.

The relatively low directivities for the four-level case come from an insufficient number of zeros. As can be seen in the two- and three-level metasurfaces, in order to suppress a diffraction channel n times throughout the Fermi level tuning we need n zeros for that given channel, unless the trajectories of zeros make a circular loop and can be 'reused' to suppress the channel again. The two- and three-level metasurfaces showcase this, as there are two zeros for the 0th channel in the two-level case to suppress it consecutively, and two zeros for each and every channel in the three-level case to suppress it for the two 'other' designated Fermi levels. However, in the four-level metasurface, we have less than three zeros for the +2nd, +1st, and −2nd channels, resulting in directivities that don't reach unity. Notice that for the 0th channel, there are indeed four zeros utilized to suppress it four times consecutively through the four Fermi levels, resulting in zero diffraction efficiencies each time.

Considering that the number of design objectives grows with the number of switching states and the number of diffraction orders, it naturally leads to the fact that it becomes increasingly more difficult to achieve higher multi-level beam switching. However, the findings reported in this analysis can be considered a preliminary result, and we suspect there might be ways to alleviate such complexities. For example, performing a larger-scale metasurface design may enable higher multi-level switching, by utilizing a larger design space and additional QNMs that could be used in sophisticated zeros shapings. In particular, we suspect expanding the metasurface design domain into 2D instead of one might overcome the problem of complicated zero shapings since 2D metasurfaces can possess more QNMs than 1D metasurfaces.

3. Conclusion

In this work, we theoretically demonstrate single-gate, electrically tunable, multi-level beam-switching metasurfaces, ranging from two to four switching levels. With the help of adjoint-based optimization, we successfully designed graphene-based active metasurfaces having both high directivities and diffraction efficiencies. For the two-level switching metasurface, the directivities reached above 98%, and the diffraction efficiencies were near 55% at the operation wavelength λ_0 = 8 μm. The operating mechanism is explained as the interference between the resonant modes and the non-resonant background modes through QNM expansion. Applying the same optimization method to the three-level switching metasurface led to above 90% directivities for all switching states. For the four-level switching metasurface design, the decline in the performance metrics raised the possibility of a fundamental trade-off/limitation on the number of switching states and the respective performances, which might be overcome by including more QNMs.

Although the results presented in this paper are based on the mid-infrared frequency regime with graphene as a tuning material, the design framework and the analysis methods can be applied to other frequency regimes and general beam-switching platforms. Especially, beam switching has an important significance in the range of millimeter waves (mmWave) for 5G communications. It is worth noting that the materials used in our work can be directly utilized in those frequency ranges as well. Graphene, the tuning material in our metasurface, is known for its high electrical tunability in those ranges, demonstrated in many works such as in broadband absorbers[70] and tunable absorbers.[71] Silicon, the material for the metal grating layer, has almost the same refractive index in those ranges.[72] Therefore, the design principle used in this work can be successfully transferred to the mmWave domain without excessive modifications. Moreover, due to the size increase in the mmWave domain, one might benefit from the easing of fabrication constraints, possibly leading to complicated nanofabrication technologies becoming redundant. We hope this work provides a useful guide in high-performance tunable beam-switching metasurface designs.

Supporting Information

Supporting Information is available from the Wiley Online Library or from the author.

Acknowledgements

This work was supported by the National Research Foundation of Korea (NRF) grants (RS-2022-NR070476, RS-2024-00416583, RS-2024-00414119) and the Institute of Information & communications Technology Planning & Evaluation (IITP) grant (RS-2024-00412644) funded by the

Korea government (MSIT). The authors also acknowledge the support by the Culture, Sports and Tourism R&D Program through the Korea Creative Content Agency grant funded by the Ministry of Culture, Sports and Tourism in 2024 (RS-2024-00332210).

Conflict of Interest

The authors declare no conflict of interest.

Author Contributions

J.P. and M.S.J. conceived the idea. J.P., J.Y.K., and M.S.J. conducted the theoretical analysis. J.P. conducted device optimizations. J.P. performed electromagnetic simulations. J.P., J.Y.K., S.N., and M.S.J. analyzed the data. J.P., J.Y.K., and M.S.J. wrote the manuscript. M.S.J. supervised the project.

Data Availability Statement

The data that support the findings of this study are available in the supplementary material of this article. We open our source code and optimized structural parameters at freely accessible repository: https://github.com/jLabKAIST/Single-Gate-Multi-Level-Beam-Switching.

Keywords

active metasurfaces, adjoint method, beam switching, free-form optimization, graphene, mid-infrared, photonic inverse design

Received: January 21, 2025
Revised: March 24, 2025
Published online: May 15, 2025

[1] B. Schwarz, *Nat. Photonics* **2010**, *4*, 429.
[2] A. Yaacobi, J. Sun, M. Moresco, G. Leake, D. Coolbaugh, M. R. Watts, *Opt. Lett.* **2014**, *39*, 4575.
[3] Feng Feng, I. H. White, T. D. Wilkinson, *J. Lightwave Technol.* **2013**, *31*, 2001,
[4] N. Yu, P. Genevet, F. Aieta, M. A. Kats, R. Blanchard, G. Aoust, *IEEE J. Sel. Top. Quantum Electron.* **2013**, *19*, 4700423.
[5] A. L. Holsteen, A. F. Cihan, M. L. Brongersma, *Science* **2019**, *365*, 257.
[6] M. Y. Shalaginov, S. An, Y. Zhang, F. Yang, P. Su, V. Liberman, J. B. Chou, C. M. Roberts, M. Kang, C. Rios, Q. Du, C. Fowler, A. Agarwal, K. A. Richardson, C. Rivero-Baleine, H. Zhang, J. Hu, T. Gu, *Nat. Commun.* **2021**, *12*, 1225.
[7] X. Zhuang, W. Zhang, K. Wang, Y. Gu, Y. An, X. Zhang, J. Gu, D. Luo, J. Han, W. Zhang, *Light: Science and Applications* **2023**, *12*, 14.
[8] L. Li, T. J. Cui, W. Ji, S. Liu, J. Ding, X. Wan, Y. B. Li, M. Jiang, C. Qiu, S. Zhang, *Nat. Commun.* **2017**, *8*.
[9] T. Gu, H. J. Kim, C. Rivero-Baleine, J. Hu, *Nat. Photonics* **2023**, *17*, 48.
[10] Y. Fan, N.-H. Shen, F. Zhang, Q. Zhao, H. Wu, Q. Fu, Z. Wei, H. Li, C. M. Soukoulis, *Adv. Opt. Mater.* **2019**, *7*, https://doi.org/10.1002/adom.201800537.
[11] V. W. Brar, M. S. Jang, M. Sherrott, J. J. Lopez, H. A. Atwater, *Nano Lett.* **2013**, *13*, 2541.
[12] M. S. Jang, V. W. Brar, M. C. Sherrott, J. J. Lopez, L. Kim, S. Kim, M. Choi, H. A. Atwater, *Phys. Rev. B* **2014**, *90*, 165409.
[13] J. Kim, G. Lee, S. G. Menabde, Y. J. Cho, C. Rockstuhl, M. S. Jang, *ACS Photonics* **2022**, *9*, 2256.
[14] J. Siegel, S. Kim, M. Fortman, C. Wan, M. A. Kats, P. W. C. Hon, L. Sweatlock, M. S. Jang, V. W. Brar, *Nat. Commun.* **2024**, *15*, 3376.
[15] V. W. Brar, M. C. Sherrott, M. S. Jang, S. Kim, L. Kim, M. Choi, L. A. Sweatlock, H. A. Atwater, *Nat. Commun.* **2015**, *6*, 7032.
[16] J. Y. Kim, J. Park, G. R. Holdman, J. T. Heiden, S. Kim, V. W. Brar, M. S. Jang, *Nat. Commun.* **2022**, *13*, 2103.
[17] S. Han, S. Kim, S. Kim, T. Low, V. W. Brar, M. S. Jang, *ACS Nano* **2020**, *14*, 1166.
[18] B. Zeng, Z. Huang, A. Singh, Y. Yao, A. K. Azad, A. D. Mohite, A. J. Taylor, D. R. Smith, H. Chen, *Light: Sci. Appl.* **2018**, *7*, 51.
[19] R. Kowerdziej, J. Wróbel, P. Kula, *Sci. Rep.* **2019**, *9*, 20367.
[20] Heiden, J. T., Jang, M. S., *Nanophotonics* **2022**, *11*, 583.
[21] P. Thureja, G. K. Shirmanesh, K. T. Fountaine, R. Sokhoyan, M. Grajower, H. A. Atwater, *ACS Nano* **2020**, *14*, 15042.
[22] M. Kang, Y. Ra'di, D. Farfan, A. Alù, *Phys. Rev. Appl.* **2020**, *13*, 044016.
[23] A. Arbabi, E. Arbabi, M. Mansouree, S. Han, S. M. Kamali, Y. Horie, A. Faraon, *Sci. Rep.* **2020**, *10*.
[24] H. Chung, O. D. Miller, *Opt. Express* **2020**, *28*, 6945.
[25] R. Paniagua-Domínguez, Y. F. Yu, E. Khaidarov, S. Choi, V. Leong, R. M. Bakker, X. Liang, Y. H. Fu, V. Valuckas, L. A. Krivitsky, A. I. Kuznetsov, *Nano Lett.* **2018**, *18*, 2124.
[26] S. Wang, P. C. Wu, V.-C. Su, Y.-C. Lai, M.-K. Chen, H. Y. Kuo, B. H. Chen, Y. H. Chen, T.-T. Huang, J.-H. Wang, R.-M. Lin, C.-H. Kuan, T. Li, Z. Wang, S. Zhu, D. P. Tsai, *Nat. Nanotechnol.* **2018**, *13*, 227.
[27] W. T. Chen, A. Y. Zhu, V. Sanjeev, M. Khorasaninejad, Z. Shi, E. Lee, F. Capasso, *Nat. Nanotechnol.* **2018**, *13*, 220.
[28] W. T. Chen, A. Y. Zhu, J. Sisler, Z. Bharwani, F. Capasso, *Nat. Commun.* **2019**, *10*, 355.
[29] M. M. R. Elsawy, S. Lanteri, R. Duvigneau, J. A. Fan, P. Genevet, Laser and Photonics Reviews, vol. *14*, **2020** Preprint at https://doi.org/10.1002/lpor.201900445.
[30] J. A. Fan, *MRS Bull.* **2020**, *45*, 196.
[31] J. Jiang, J. A. Fan, *Nanophotonics* **2019**, 1059.
[32] H. Chung, O. D. Miller, *ACS Photonics* **2020**, *7*, 2236.
[33] Y. Zhou, S. Guo, A. C. Overvig, A. Alu, *Nano Letters* **2023**, *23*, 6768.
[34] D. Sell, J. Yang, S. Doshay, R. Yang, J. A. Fan, *Nano Letters* **2017**, *17*, 3752.
[35] C. Park, S. Kim, A. W. Jung, J. Park, D. Seo, Y. Kim, C. Park, C. Y. Park, M. S. Jang, *Nanophotonics* **2024**, *13*, 1483.
[36] D. Seo, D. W. Nam, J. Park, C. Y. Park, M. S. Jang, *ACS Photonics* **2021**, *9*, 452.
[37] F. Binkowski, F. Betz, R. Colom, P. Genevet, S. Burger, *Phys. Rev. B* **2024**, *109*, 45414.
[38] P. Gonccalves, N. M. R. Peres, *arXiv: Mesoscale and Nanoscale Physics* **2016**.
[39] C. A. Dirdal, G. U. Jensen, H. Angelskår, P. C. Vaagen Thrane, J. Gjessing, D. A. Ordnung, *Opt. Express* **2020**, *28*, 15542.
[40] J. Parasuraman, A. Summanwar, F. Marty, P. Basset, D. E. Angelescu, T. Bourouina, *Microelectron. Eng.* **2014**, *113*, 35.
[41] A. Wratten, D. Walker, E. Khorani, B. F. M. Healy, N. E. Grant, J. D. Murphy, *AIP Advances* **2023**, *13*, 065113.
[42] K. S. Min, B. J. Park, S. W. Kim, S. K. Kang, G. Y. Yeom, S. H. Heo, H. S. Hwang, C. Y. Kang, *Journal of the Korean Physical Society* **2008**, *53*, 1675.
[43] J. P. Mailoa, A. J. Akey, C. B. Simmons, D. Hutchinson, J. Mathews, J. T. Sullivan, D. Recht, M. T. Winkler, J. S. Williams, J. M. Warrender, P. D. Persans, M. J. Aziz, T. Buonassisi, *Nat. Commun.* **2014**, *5*, 3011.
[44] S. Kol, A. Y. Oral, *Acta Phys. Pol. A* **2019**, *136*, 873.
[45] C. Sire, S. Blonkowski, M. J. Gordon, T. Baron, *Appl. Phys. Lett.* **2007**, *91*, 242905.
[46] S. Kim, C. Park, S. Kim, H. Chung, M. S. Jang, *Iscience* **2023**, *26*, 107788.
[47] J. Park, S. Kim, J. Lee, S. G. Menabde, M. S. Jang, *Phys. Rev. Appl.* **2019**, *12*, 024030.

[48] S. Kim, J. M. Shin, J. Lee, C. Park, S. Lee, J. Park, D. Seo, S. Park, C. Y. Park, M. S. Jang, *Nanophotonics* **2021**, *10*, 4533.
[49] J. Jiang, J. A. Fan, *Nano letters* **2019**, *19*, 5366.
[50] M. Mansouree, H. Kwon, E. Arbabi, A. McClung, A. Faraon, A. Arbabi, *Optica* **2020**, *7*, 77.
[51] T. Phan, D. Sell, E. W. Wang, S. Doshay, K. Edee, J. Yang, J. A. Fan, *Light: Science & Applications* **2019**, *8*, 48.
[52] J. Park, S. Kim, D. W. Nam, H. Chung, C. Y. Park, M. S. Jang, *Nanophotonics* **2022**, *11*, 1809.
[53] O. D. Miller, *Photonic Design: From Fundamental Solar Cell Physics to Computational Inverse Design*, University of California, Berkeley, **2012**.
[54] M. Zadka, Y.-C. Chang, A. Mohanty, C. T. Phare, S. P. Roberts, M. Lipson, *Opt. Express* **2018**, *26*, 2528.
[55] J. D. Joannopoulos, S. G. Johnson, J. N. Winn, R. D. Meade, *Molding the flow of light*, Princeton University Press, Princeton, NJ, Vol. *12*, **2008**.
[56] E. S. C. Ching, P. T. Leung, A. M. Brink, W. M. Suen, S. S. Tong, K. Young, *Rev. Mod. Phys.* **1998**, *70*, 1545.
[57] B. Vial, F. Zolla, A. Nicolet, M. Commandre, *Phys. Rev. A* **2014**, *89*, 23829.
[58] F. Zolla, A. Nicolet, G. Demesy, *Opt. Lett.* **2018**, *43*, 5813.
[59] W. Yan, R. Faggiani, P. Lalanne, *Phys. Rev. B* **2018**, *97*, 205422.
[60] F. Betz, F. Binkowski, S. Burger, *SoftwareX* **2021**, *15*, 100763.
[61] L. Zschiedrich, F. Binkowski, N. Nikolay, O. Benson, G. Kewes, S. Burger, *Phys. Rev. A* **2018**, *98*, 43806.
[62] P. D. Hislop, I. M. Sigal, *Introduction to Spectral Theory: With Applications to Schrödinger Operators*, Vol. *113*, Springer Science & Business Media, Berlin, **2012**.
[63] V. Liu, S. S. Fan, *Comput. Phys. Commun.* **2012**, *183*, 2233.
[64] M. Born, E. Wolf, *Principles of Optics: Electromagnetic Theory of Propagation, Interference and Diffraction of Light*, Elsevier, Amsterdam, **2013**.
[65] L. A. Falkovsky, *J. Phys.: Conf. Ser.* **2008**, *129*, 12004.
[66] S.-P. Han, *Journal of Optimization Theory and Applications* **1977**, *22*, 297.
[67] P. E. Gill, W. Murray, M. H. Wright, *Practical Optimization*, SIAM, Philadelphia, PA, **2019**.
[68] R. Colom, E. Mikheeva, K. Achouri, J. Zuniga-Perez, N. Bonod, O. J. F. Martin, S. Burger, P. Genevet, *Laser Photonics Rev.* **2023**, *17*, 2200976.
[69] E. Mikheeva, R. Colom, K. Achouri, A. Overvig, F. Binkowski, J. Duboz, S. Cueff, S. Fan, S. Burger, A. Alu, P. Genevet, *Optica* **2023**, *10*, 10.
[70] B. Wu, H. M. Tuncer, M. Naeem, B. Yang, M. T. Cole, W. I. Milne, Y. Hao, *Sci. Rep.* **2014**, *4*.
[71] A. D. Squires, X. Gao, J. Du, Z. Han, D. H. Seo, J. S. Cooper, A. T. Murdock, S. K. H. Lam, T. Zhang, T. Laan, *Commun. Mater.* **2022**, *3*.
[72] D. Franta, P. Franta, J. Vohanka, M. Cermak, I. Ohlidal, *J. Appl. Phys.* **2018**, *123*, 185707.